International Journal of Minerals, Metallurgy and Materials
Volume 25, Number 5, May 2018, Page 505
https://doi.org/10.1007/s12613-018-1597-4

Mineral structure and crystal morphologies of high-iron hydrargillite

Hui-bin Yang[1)], *Feng-qin Liu*[2)], *and Xiao-lin Pan*[3)]

1) Hangzhou Yinsheng Enterprise Management Co., Ltd., Hangzhou 310007, China

2) School of Metallurgical and Ecological Engineering, University of Science and Technology Beijing, Beijing 100083, China

3) School of Metallurgy, Northeastern University, Shenyang 110819, China

(Received: 24 October 2017; revised: 27 December 2017; accepted: 10 January 2018)

Abstract: Various characterization methods, including scanning electron microscopy, transmission electron microscopy, energy-dispersive X-ray spectroscopy, Brunauer–Emmett–Teller surface-area measurements, thermogravimetry–differential scanning calorimetry, X-ray diffraction, and infrared spectroscopy, were used to study the mineral structure and surface characteristics of high-iron hydrargillite. Gibbsite, goethite, and hematite were found to be the main mineral components of hydrargillite, whereas the goethite and hematite were closely clad to the surface of the multilayer gibbsite crystals. Compared with the synthetic gibbsite, the hydrargillite contained more structural micropores generated by the mineral evolution during the mineralization process. The gibbsite in hydrargillite contained less crystal water compared with the synthetic gibbsite, and it was a typical polymorphic structure. The isomorphous substitution of Al and Fe was observed in goethite. The dissolution-controlling step of hydrargillite was the ionic diffusion speed because of the goethite and hematite that closely covered and encapsulated the gibbsite crystals.

Keywords: hydrargillite; goethite; gibbsite; mineral structure; crystal morphologies

1. Introduction

Bauxite is the raw material of metallurgical-grade alumina and hydrargillite has the largest reserves, making hydrargillite the main raw material for current worldwide alumina production. The mineralization process of hydrargillite requires special geological conditions, which include a long period of heavy rainwater and infiltration. Therefore, hydrargillite is generally found in high-temperature, high-rainfall, and high-humidity equatorial or low-latitude regions such as Indonesia, India, Vietnam, and Guinea. The mother rocks of hydrargillite are feldspar, plagioclase, mica, etc. [1–3], whereas pyroxene is the mother rock of hematite and goethite. After weathering, pyroxene produces goethite and then becomes hematite under certain external conditions. Hematite is the final ferrous mineral of the weathering of iron-bearing rock [2]. Pyroxene and plagioclase are paragenetic minerals; therefore, goethite and hematite become the major associated minerals in hydrargillite, along with the process of geological evolution. High-iron hydrargillite deposits can be formed when a large proportion of pyroxene ore exists in the mother rock of hydrargillite. Because of the combination of large quantities of iron minerals with gibbsite crystals and the similar atomic radii of Fe and Al, isomorphism is often observed in hydrargillite.

The bauxite structure provides the theoretical basis for ore resource exploration and for research of the dissolution mechanism. According to the hydrargillite structure of Guangxi and Guizhou, Qian *et al.* [4] analyzed the formation characteristic of hydrargillite. Guangxi hydrargillite has a clastic and colloidal structure arising from the very placid sedimentary water, and the crusty particles in the ore are formed by colloidization in the penecontemporaneous period. Guizhou hydrargillite assumes oolitic bean shapes and a clastic structure and is formed because of the $A1(OH)_3$ colloid that is continuously deposited around the granule or the colloidal mass in the turbulent water environment. Chen *et al.* [5] studied the structure of two kinds of karst hydrargillite in Guangxi. Their results show that the gibbsite in the ore has plate or flake structures, the goethite is a kidney-shaped, crusty, oolitic bean aggregate, and the isomorphous replacement amount of Al and Fe is

Corresponding author: Feng-qin Liu E-mail: liufq@ustb.edu.cn

20wt%–24wt%. Zhang *et al.* [6] studied the structure of a bauxite-bearing rock series in southeastern Guizhou. Their results show that, in this case, hydrargillite is mainly composed of oolitic bean particles and contains clastic and earthy particles. The ore shapes reflect the process of water transport and deposition; for example, gibbsite was brought into the shallow sea by water and formed oolitic, lenticular, and tubercular ore particles by colloid agglomeration. Bao *et al.* [7] studied the structure changes of gibbsite during the dissolution process. With extension of the dissolution time, the specific area and pore volumes of gibbsite particles first increased and then decreased and the particle surface structure gradually became loose.

The study of hydrargillite structure is important for research of its dissolution process in alkali aqueous solutions and for improving alumina technology. It also may benefit and guide the comprehensive utilization of red mud and hydrargillite resource exploration. For the alumina industry, the study of the hydrargillite structure will aid in optimizing the dissolution process; in addition, reasonable ore crushing granularity and alkali concentrations can be adopted to shorten the dissolution process and improve the dissolution efficiency. In the exploration of mineral resources, the metallogenic evolution process can be evaluated on the basis of the hydrargillite structure, which can then provide clues and directions for ore resource exploration. The structure of red mud can also be estimated according to the ore structure, which will provide theoretical support for the comprehensive utilization of red mud.

2. Experimental

2.1. Test materials

The high-iron hydrargillite used in this work was obtained from Kalimantan, Indonesia, which is near the Equator. Kalimantan has a tropical rainforest climate with high temperatures, high humidity, and abundant rainfall, providing good natural metallogenic conditions for hydrargillite. The sample is typical laterite hydrargillite and is broadly representative. The sample was dried at 105°C for 6 h and then crushed by a jaw crusher and roll-crushing mill. The particle size of the final sample was between 0.5 and 1.0 mm. The chemical components of the sample are shown in Table 1. The main components are Fe_2O_3 and Al_2O_3, composing a total of 70.33wt% of the sample.

Table 1. Main chemical components of high-iron hydrargillite

wt%

SiO_2	Fe_2O_3	Al_2O_3	TiO_2	Loss on ignition
2.78	31.03	39.30	1.01	22.60

The synthetic gibbsite used in this research was $Al(OH)_3$ obtained from an alumina industry process. The sample was dried at 105°C for 3 h. The particle size of the sample was between 75 and 100 μm.

2.2. Test instruments and analysis methods

A D8 ADVANCE X-ray diffractometer with a Cu target cathode was used for the X-ray diffraction (XRD) analysis of the samples. The voltage was 30 kV, the current was 15 mA, the scanning angle was varied from 0° to 75°, the step size was 0.02°, and the scanning speed was 4°/min.

Scanning electron microscopy (SEM) observations of the samples were performed on a S4800 cold field-emission scanning electron microscope equipped with an energy-dispersive X-ray spectroscopy (EDS) apparatus. The resolution ratio was 1.00 nm (15 kV), and the acceleration voltage was 0.50 to 30 kV.

Transmission electron microscopy (TEM) analysis was performed using a Tecnai G2 F30 equipped with EDS and a charge-coupled device (CCD) camera digital recording system. The acceleration voltage, point resolution, line resolution, and image resolution were 300 kV, 0.20 nm, 0.10 nm, and 0.17 nm, respectively.

Thermogravimetry (TG) and differential scanning calorimetry (DSC) were performed on an STA 449F3 super-high-temperature synchronous heat analyzer. The TG sensitivity was 0.10 μg, and the DSC sensitivity was less than 1 μW. The test atmosphere was nitrogen, the heating rate was 10°C/min, and the testing range was 30–1350°C.

The infrared (IR) spectra were obtained using a Fourier transform infrared spectrometer. The frequency range was 400 to 25000 cm^{-1}, and the resolution was 1 cm^{-1}.

The Brunauer–Emmett–Teller (BET) specific surface area was measured using a V-Sorb 2800P specific surface area and aperture analyzer. The specific surface area measurement range was greater than 0.01 m^2/g, and the aperture measurement range was 0.35–400 nm.

Chemical components of the samples were analyzed according to the appropriate national standard or professional standard.

3. Results and discussion

3.1. Mineral composition of the hydrargillite

The XRD pattern of the hydrargillite sample is shown in Fig. 1. The main mineral compositions are gibbsite, goethite, and hematite. The silicon-containing minerals are quartz and kaolinite. In addition, a small amount of anatase also appears in the XRD pattern.

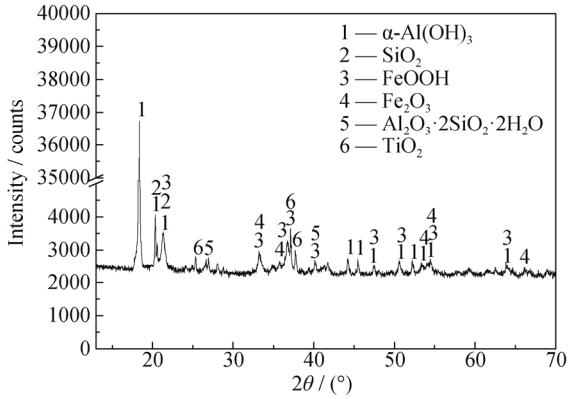

Fig. 1. XRD pattern of hydrargillite.

The diffraction data of gibbsite and the corresponding standard card data are shown in Table 2. As shown in Table 2, the lower relative intensities of the (110) and (200) peaks indicate that the sample is poorly crystalline. The interplanar spacings of the (002) and (110) planes are almost the same as those reported in the standard card. The (200) interplanar distance of the sample is smaller, which, in conjunction with the 2θ shift, suggests that the crystal unit cell of the gibbsite in hydrargillite is smaller than that of standard gibbsite.

Table 2. XRD data for the three most intense peaks of gibbsite

Item	2θ / (°)	Crystal orientation	Intensity / %	Interplanar distance / nm
Sample	18.24	(002)	100.00	0.4858
	20.31	(110)	8.92	0.4369
	21.24	(200)	5.77	0.4180
Standard card	18.28	(002)	100.00	0.4850
	20.31	(110)	16.00	0.4370
	20.54	(200)	8.00	0.4320

3.2. Micromorphology and structure of the hydrargillite

SEM images of the high-iron hydrargillite are shown in Fig. 2. The crystal particles show various shapes, including flaky crystals, multilayer chip crystals, and clava particles covered with abundant patchy particles. Different morphologies in hydrargillite may represent different minerals. The high-iron hydrargillite is mainly composed of gibbsite, hematite, and goethite. Therefore, the various crystal particles in hydrargillite should arise mainly from these three minerals.

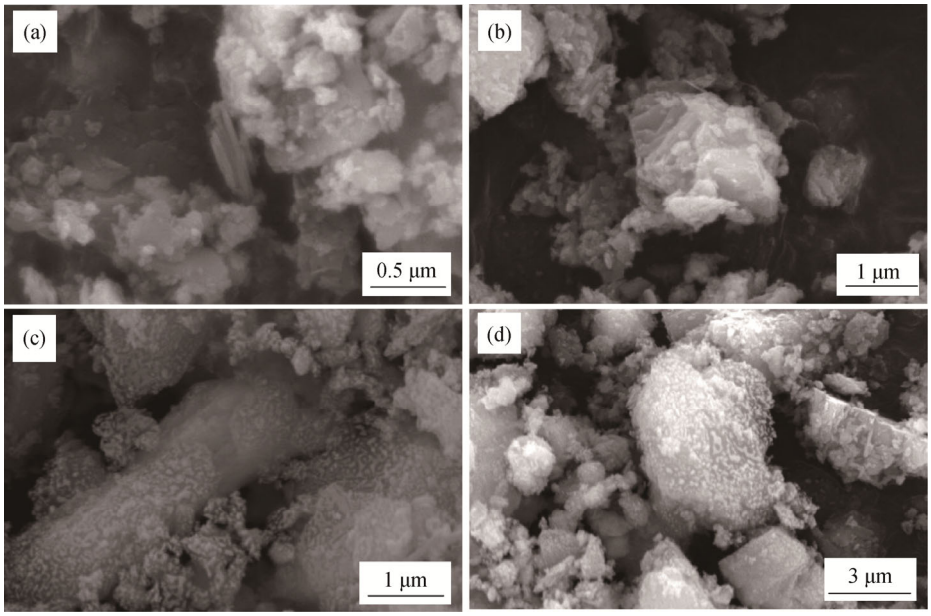

Fig. 2. SEM images of the high-iron hydrargillite: (a) flaky; (b) multilayer tablet; (c) clava particles and the spot layer; (d) lump and the spot layer.

Crystalline gibbsite has been reported to exist in a dispersed cryptocrystalline or microcrystalline form, and the crystal particles are false six-square plate, sheet, or scaly flaky shapes; goethite and alumogoethite exhibit kidney, crusty, or oolitic aggregate shapes [5].

The EDS analysis results for different particle morphologies are shown in Figs. 3–5 and Tables 3–5. The results presented in these tables and figures show that Fe and Al exist in various particles, which can indicate two conditions: (1) iron-bearing minerals extensively mixed with gibbsite crystals and (2) a large number of isomorphous substitutions of Al and Fe in the goethite. The Fe content of the clava particles is relatively higher, indicating that the minerals are hematite, goethite, or alumogoethite, as shown in Fig. 3

(point 2) and Table 3. The Al content in flaky lamellar and flaky-lump crystals is higher, indicating that the crystal shape of the gibbsite is flaky; however, most of the gibbsite crystals are mixed together with other minerals and almost no crystal particles are present in a pure state, as shown in Figs. 4–5 and Tables 4–5. The minerals containing Si and Ti do not form separate crystal particles because of their low content in the ore.

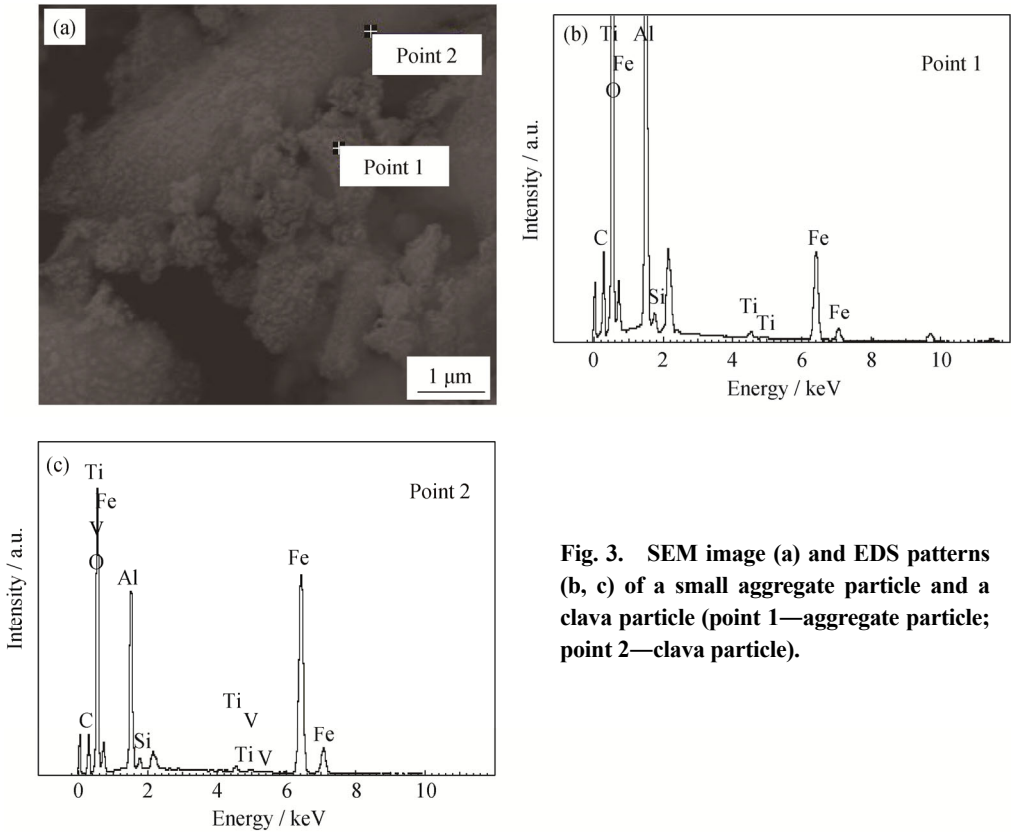

Fig. 3. SEM image (a) and EDS patterns (b, c) of a small aggregate particle and a clava particle (point 1—aggregate particle; point 2—clava particle).

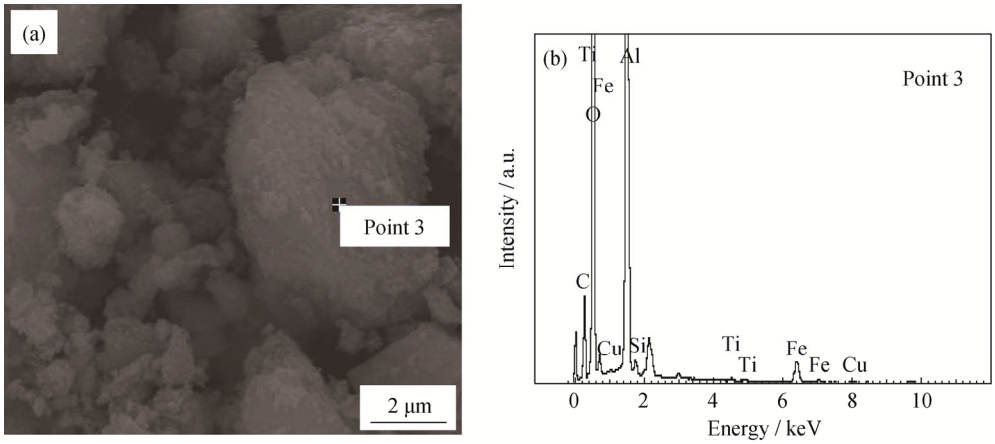

Fig. 4. SEM image (a) and EDS pattern (b) of a layered particle.

The high-iron hydrargillite was also analyzed by TEM and EDS; the results are shown in Fig. 6. In TEM dark-field images, brighter regions indicate the regions of the higher-density mineral. Combining the TEM with the XRD and chemical composition analysis results reveals that the higher-density minerals are goethite or hematite, as shown in Figs. 6(a) and 6(b). The gibbsite crystal is found in a flake or lamellar shape, and the superimposed multilayered lamellar crystals form the gibbsite crystal particles. The crystal surface is covered with goethite minerals, forming a cladding layer, which is the main structural form of the high-iron hydrargillite, as shown in Fig. 6(b). The high-resolution TEM images of gibbsite crystals

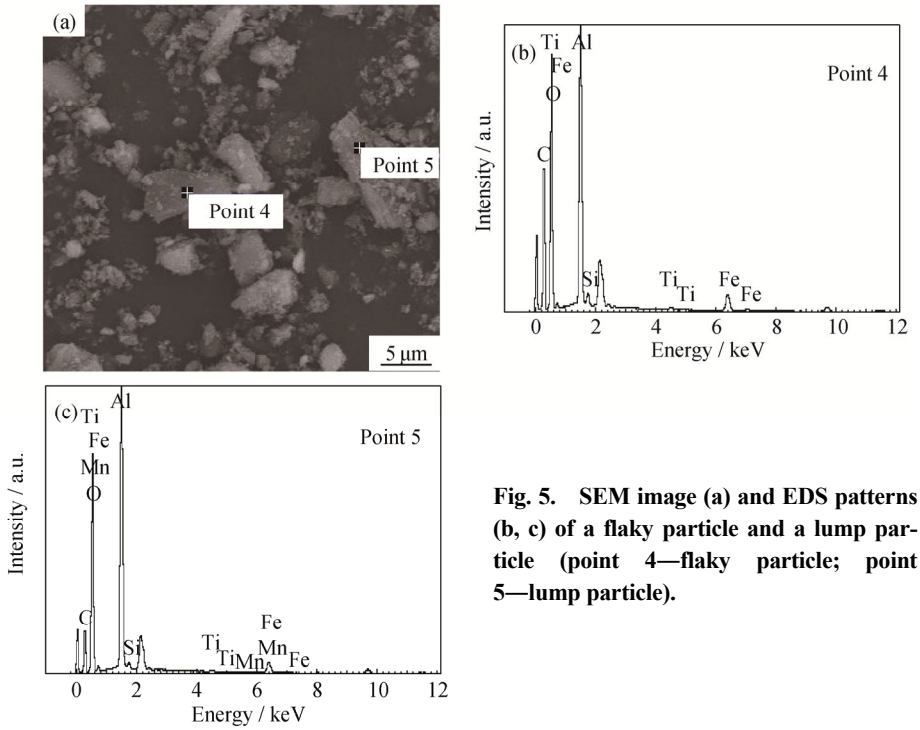

Fig. 5. SEM image (a) and EDS patterns (b, c) of a flaky particle and a lump particle (point 4—flaky particle; point 5—lump particle).

show that the crystal direction is scattered, and the transmission spot is broadened, with different distances overlapping each other. Therefore, gibbsite exhibits a typical polymorphic structure, as shown in Figs. 6(c) and 6(d).

Table 3. Elemental content of an aggregate particle and a clava particle wt%

Test point	O	Al	Si	Ti	V	Fe
Point 1	64.11	21.36	0.62	0.44	0	13.47
Point 2	41.63	11.45	0.63	0.67	0.23	45.39

Table 4. Elemental content of a layered particle wt%

Test point	O	Al	Si	Ti	Fe	Cu
Point 3	68.07	28.19	0.45	0.21	2.88	0.21

Table 5. Elemental content of a flaky particle and a lump particle wt%

Test point	O	Al	Si	Ti	Mn	Fe
Point 4	73.77	20.20	0.67	0.35	0	5
Point 5	67.62	27.22	0.57	0.25	0.32	4.03

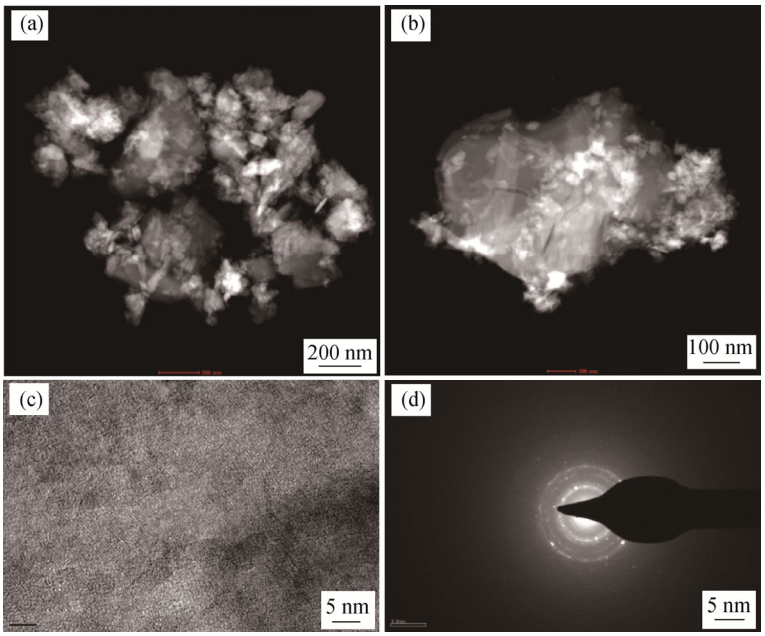

Fig. 6. TEM images of high-iron hydrargillite: (a) dispergated particles; (b) single particle; (c) high-resolution image; (d) image of transmission spots.

The TEM and EDS analysis results for particles smaller than 1.0 μm are shown in Fig. 7 and Table 6. The results show that the main elements are O and Fe, composing a total of 95.14wt% of the sample. In combination with the XRD analysis results, these findings confirm that the mineral particles are goethite, which is abundant in the hydrargillite. No flaky structure appears in the particles containing Al, indicating the isomorphous substitution of Al and Fe in goethite.

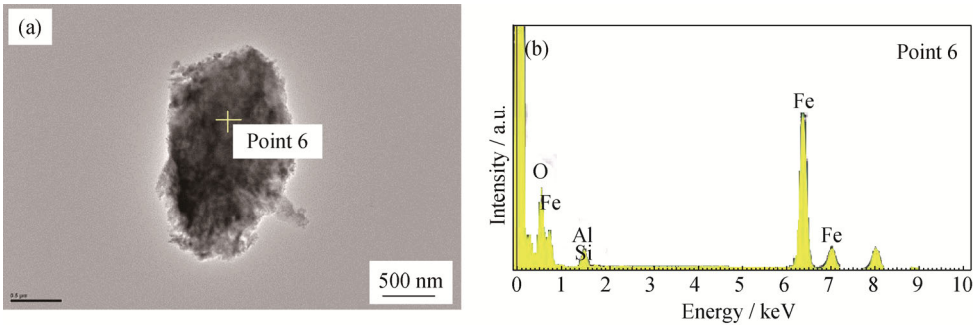

Fig. 7. TEM image (a) and EDS pattern (b) of a small particle.

Table 6. Elemental content of a small particle wt%

Test point	O	Al	Si	Fe
Point 6	30.22	4.12	0.74	64.92

3.3. IR characteristics of the hydrargillite

IR analysis can help determine the mineral species and the crystalline state. The IR analysis results of synthetic gibbsite and high-iron hydrargillite are shown in Fig. 8. The synthetic gibbsite is a pure gibbsite crystal; its characteristic IR peaks are shown in Fig. 8. The obtained spectrum is consistent with previously reported data [8]. The absorption peaks between 3700 and 3000 cm^{-1} are assigned mainly to the symmetrical and asymmetric stretching vibration peaks of water molecules, indicating that crystalline water is present in the hydrargillite. The crystalline water content is less than that of synthetic gibbsite. The absorption peak located at 1016.57 cm^{-1} is the Al–OH vibration peak, and the peaks located at 910.76 and 795.55 cm^{-1} are Fe–OH vibration peaks indicating the presence of goethite.

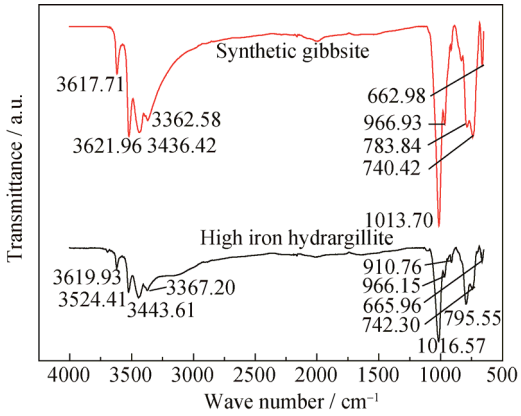

Fig. 8. IR patterns of high-iron hydrargillite and synthetic gibbsite.

The characteristic absorption peaks of kaolinite have been reported to be located at 3697 and 3621 cm^{-1} [9–10]. The two kaolinite peaks do not appear in the spectra because of its low content and highly dispersed state.

3.4. TG–DSC characteristics of the hydrargillite

The mass loss and enthalpy change during the heating process were analyzed by TG–DSC. The analysis results of synthetic gibbsite and high-iron hydrargillite are shown in Figs. 9 and 10, respectively.

As shown in Fig. 9, two endothermic peaks appear in the DSC curve. The first peak occurs at 302.6°C, and its absorption heat is 1010.80 J/g, representing the loss of gibbsite crystal water. The second peak occurs at 529.4°C, and its absorption heat is 106.60 J/g.

The dehydration reaction of crystal water with poor crystallization is priority. In the temperature region from 228.8 to 529.4°C, the difference in the mass-loss rates and absorption heat of endothermic peaks indicates the removal process of crystal water with different degrees of crystallization.

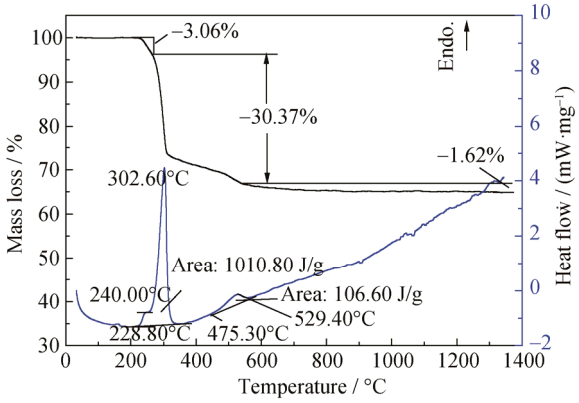

Fig. 9. TG–DSC patterns of synthetic gibbsite.

As shown in Fig. 10, an obvious endothermic peak appears at 300.2°C accompanied by a mass loss, corresponding to the dehydration reaction of the gibbsite. Whereas the dehydration of goethite can also produce an endothermic peak and mass loss, only one endothermic peak is present in the curve, indicating that the dehydration temperature of goethite is approximately the same as that of gibbsite, which leads to the overlap of the two endothermic peaks. The heat absorption capacity per unit mass of high-iron hydrargillite at 300.2°C is much lower than that of synthetic gibbsite, indicating a lower crystal water content. Only one obvious endothermic peak is present in the curve, indicating the faster removal rate of crystal water in hydrargillite.

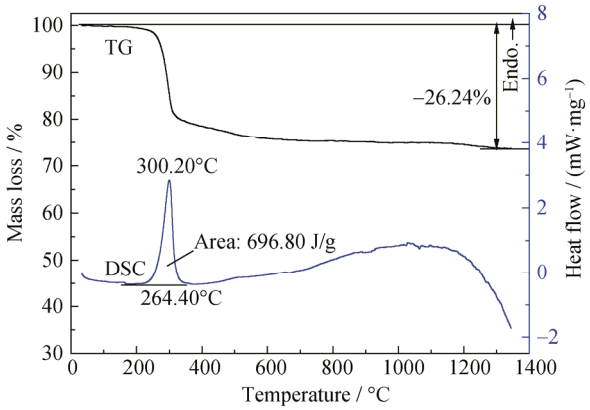

Fig. 10. TG–DSC curves of high-iron hydrargillite.

3.5. Specific surface and pore structural characteristics of the hydrargillite

To study pore structure and microsurface characteristics of the high-iron hydrargillite, we investigated its specific surface area and pore size. This information is helpful for understanding the liquid–solid interface reaction between hydrargillite and an alkaline solution. Additionally, it will be helpful in the selection of an appropriate reaction model.

The pretreatment temperature of the sample was 100°C to ensure that the original structural properties of the sample were maintained. This low treatment temperature can avoid possible changes of the surface or pore structure characteristics as a result of the loss of crystal water.

The adsorption isotherms of the hydrargillite are shown in Fig. 11. These results show that the adsorption interaction between nitrogen and the hydrargillite is very weak and this adsorption capacity may be less than that between nitrogen molecules. It also indicates that the pore-filling phenomenon of the nitrogen gas in the micropore occurs under high-pressure conditions. In the low-pressure zone, the adsorption line does not duplicate the desorption line, indicating that numerous micropores exist in the hydrargillite. The desorption hysteresis phenomenon occurred because of the capillary condensation.

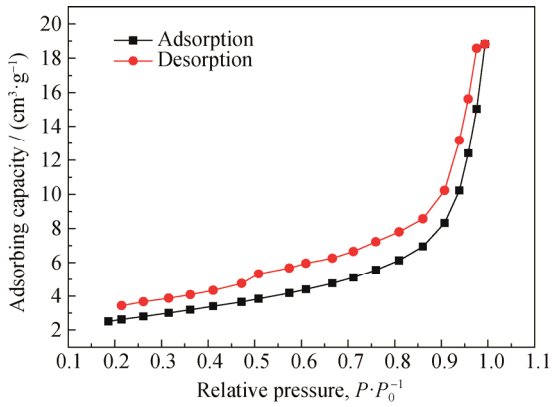

Fig. 11. Isotherms absorption curves of high-iron hydrargillite (*P* is the testing pressure and P_0 is the atmospheric pressure).

The specific surface area values of the high-iron hydrargillite obtained by different calculation methods are shown in Table 7. The calculated deviation of single-point BET is relatively large, the Langmuir method is suitable for the calculation of the specific surface area of a monomolecular layer. Therefore, the measured values of the multipoint BET specific surface area were selected in this work. The specific surface area of the high-iron hydrargillite was 9.26 cm^2/g.

Table 7. Specific surface area of high-iron hydrargillite obtained by different calculation methods $cm^2 \cdot g^{-1}$

Single-point BET	Multipoint BET	Langmuir
9.00	9.26	12.57

The pore volume values obtained by different calculation methods are shown in Table 8. The highest single-point adsorption volume was 0.03 cm^3/g. The pore diameters obtained by different calculation methods are shown in Table 9. Generally, the average pore diameter of the single-point total hole adsorption is widely adopted; it was 12.57 nm in the present work.

Table 8. Pore volume of high-iron hydrargillite $cm^3 \cdot g^{-1}$

Highest single-point adsorption total pore volume	Saito–Foley total micropore volume
0.03	0.005

Table 9. Pore diameter of high-iron hydrargillite nm

Single-point total hole adsorption average pore diameter	Saito–Foley middle pore diameter
12.57	0.91

To attain a better understanding of the structural characteristics of high-iron hydrargillite, we analyzed two kinds of synthetic gibbsite; the results are shown in Table 10. The values of the specific surface area, pore volume, and pore diameter of the carbonation-precipitation synthetic gibbsite are larger than those of the seeded-precipitation synthetic gibbsite, indicating that the structure of the seeded-precipitation-synthesized gibbsite is more dense.

Table 10. Specific surface area, pore volume, and pore diameter of synthetic gibbsite

Sample	Multipoint BET specific surface area / ($cm^2 \cdot g^{-1}$)	Highest single-point adsorption total pore volume / ($cm^3 \cdot g^{-1}$)	Single-point total hole adsorption average pore diameter / nm
Carbonation-precipitation-synthesized gibbsite	0.52	0.01	76.85
Seeded-precipitation-synthesized gibbsite	0.20	0.002	41.57

Compared with synthetic gibbsite, the specific surface area and pore volume of the high-iron hydrargillite are larger, whereas the average pore diameter of the high-iron hydrargillite is smaller. These results show that the pores of synthetic gibbsite are mainly intercrystal pores formed in the crystal agglomeration process; thus, the pore diameter is larger but few micropores are present in the individual crystal particles. The high-iron hydrargillite undergoes mineral evolution in the mineralization process, along with changes of the mineral species, giving rise to its structural change and leading to the formation of more structural micropores.

3.6. Effect of structure on dissolution properties

Because of the higher crystallinity of synthetic gibbsite, the dissolution process is relatively simple and not affected by other factors; studies of gibbsite dissolution are generally based on synthetic gibbsite [11–17]. In the study of gibbsite dissolution, the control step is generally evaluated according to the activation energy and the appropriate dynamic equation [18–19]. Pereira *et al.* [13] found that the dissolution of gibbsite was controlled by chemical reactions, whereas Yin *et al.* [16] argued that the control steps differ at different stages of dissolution. Overall, most researchers consider the dissolution process of synthetic gibbsite under atmospheric pressure to be dominated by chemical reactions.

High-iron hydrargillite has a dissolution mechanism that differs from that of synthetic gibbsite. Studies of the dissolution of high-iron hydrargillite in alkaline solutions under atmospheric pressure have shown that diffusion is the dissolution-controlling step [20–22]. The dissolution kinetics equations are shown as Eqs. (1) and (2), which represent reaction rates controlled by the chemical reaction and by the diffusion process, respectively [18–19]:

$$1-(1-\alpha)^{1/3} = kt \quad (1)$$

$$1-2\alpha/3-(1-\alpha)^{2/3} = kt \quad (2)$$

where α is the dissolution efficiency of Al_2O_3, k is the apparent rate constant of gibbsite, and t is the dissolution time.

The linear relationship coefficients of Eqs. (1) and (2) are shown in Fig. 12, where the linear relationships between $1-2\alpha/3-(1-\alpha)^{2/3}$ and t indicate that the limiting step of dissolution is the diffusion process. This result is mainly attributable to the structural difference between synthetic gibbsite and high-iron hydrargillite. Synthetic gibbsite is a pure gibbsite mineral, and the diffusion of reactants and products is relatively fast; thus, the chemical reaction is the limiting step. According to the results of this study, the

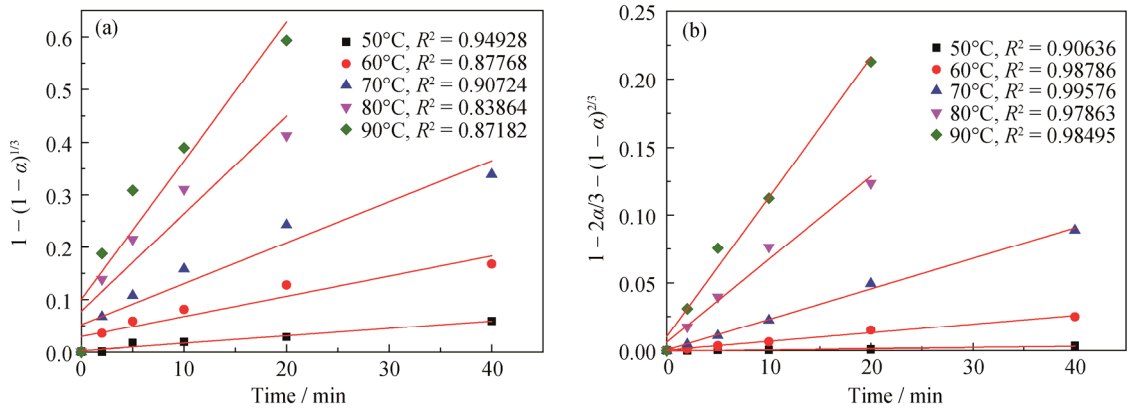

Fig. 12. Dissolution rate curves of high-iron hydrargillite (experimental conditions: sample particle median size of 0.75 mm, reaction temperature of 50–90°C, stirring speed of 350 r/min, NaOH concentration of 3 mol/L, and solid concentration of 100 g/L): (a) $1-(1-\alpha)^{1/3}$ vs. t; (b) $1-2\alpha/3-(1-\alpha)^{2/3}$ vs. t.

gibbsite crystals in the hydrargillite are closely covered and encapsulated by a large number of iron minerals, as shown in Fig. 2 and Figs. 6(a) and 6(b). This encapsulation strongly affects the diffusion rates of reactants and products, leading to the dissolution reaction rate of the high-iron hydrargillite being controlled by diffusion.

4. Conclusions

(1) The gibbsite crystals of the high-iron hydrargillite assumed flaky, multilayer, and lump lamellar shapes, and the gibbsite was polycrystalline. Goethite and hematite assumed the shapes of dispersed granular or clava particles. Goethite and hematite were closely attached to the surface of the gibbsite crystal, forming a cladding layer.

(2) In the IR spectrum, the Al–OH vibration peak appeared at 1016 cm^{-1}, and the Fe–OH shock peaks appeared at 910 and 795 cm^{-1}, except for the flexible vibration peak arising from the crystallized water, which reflects the presence of gibbsite and goethite in the hydrargillite.

(3) TG–DSC experiments showed that the dehydration temperature of goethite was basically the same as that of gibbsite and the endothermic peaks of these two materials overlapped.

(4) The specific surface area and pore volume of the high-iron hydrargillite were 9.26 cm^2/g and 0.03 cm^3/g, respectively. The presence of micropores in the hydrargillite resulted in capillary condensation and desorption hysteresis during the isothermal nitrogen adsorption. Compared with synthetic gibbsite, high-iron hydrargillite exhibited a larger specific surface area but a smaller pore diameter.

(5) Because of the effects of structural characteristics, high-iron hydrargillite and synthetic gibbsite showed different dissolution-controlling steps. The chemical reaction was the controlling step for the synthetic gibbsite, whereas diffusion was the controlling step for the high-iron hydrargillite in an alkaline solution under atmospheric pressure.

Acknowledgement

This work was financially supported by the National Natural Science Foundation of China (No. 51104041).

References

[1] G. Certini, M.J. Wilson, S.J. Hillier, A.R. Fraser, and E. Delbos, Mineral weathering in trachydacitic-derived soils and saprolites involving formation of embryonic halloysite and gibbsite at Mt. Amiata, Central Italy, *Geoderma*, 133(2006), No. 3-4, p. 173.

[2] L. Herrmann, N. Anongrak, M. Zarei, U. Schuler, and K. Spohrer, Factors and processes of gibbsite formation in Northern Thailand, *Catena*, 71(2007), No. 2, p. 279.

[3] B. Mulyanto, G. Stoops, and E.V. Ranst, Precipitation and dissolution of gibbsite during weathering of andesitic boulders in humid tropical West Java, Indonesia, *Geoderma*, 89(1999), No. 3-4, p. 287.

[4] L.J. Qian, G. Wang, L.H. Ou, and X. Hu, Contrast of structure characteristics and sedimentary environment of sedimentary bauxite deposit in Pingguo Guangxi and Qingzhen Guizhou, *Sci. Technol. Eng.*, 16(2016), No. 4, p. 135.

[5] J.G. Chen, Y.H. Liu, and J.W. Xu, Differences of mineralization of two gibbsite bauxites in Guangxi province, *Earth Sci. Front.*, 6(1999), Supp. 1, p. 251.

[6] Z.W. Zhang, Y.J. Li, L.J. Zhou, and C.Q. Wu, Coal-bauxite-iron structure and geochemical features of bauxites ore-bearing rock series in southeast Guizhou, *Acta Geol. Sin*., 86(2012), No. 7, p. 1119.

[7] L. Bao, T.A. Zhang, G.Z. Lv, and Z.H. Dou, Microstructural change of gibbsite particle in digestion process, *J. Northeast. Univ. Nat. Sci.*, 31(2010), No. 10, p. 1453.

[8] S. Wang, N. Wang, C.L. Li, J.J. Zhang, and S. Dou, FTIR Spectroscopic analysis of Cu^{2+} adsorption on hematite and bayerite, *Spectrosc. Spect. Anal.*, 31(2011), No. 9, p. 2403.

[9] S.C. Hu, H.Q. Zhao, H.L. Ma, and Y. Zhang, Normal atmosphere digestion tests on gibbsite of Hai-nan province, *Min. Metall. Eng.*, 32(2012), No. z1, p. 107.

[10] S.C. Hu, H.B. Wang, H.Q. Zhao, H.L. Ma, and B.J. Zhao, Normal atmosphere digestion tests on low alumina to silica ratio and high iron gibbsite bauxite, *Conserv. Utiliz. Miner. Resour.*, 2011, No. 1, p. 60.

[11] X.B. Li, D.F. Zhao, S.S. Yang, D.Q. Wang, Q.S. Zhou, and G.H. Liu, Influence of thermal history on conversion of aluminate species in sodium aluminate solution, *Trans. Nonferrous Met. Soc. China*, 24(2014), No. 10, p. 3348.

[12] X.B. Li, L. Yan, Q.S. Zhou, G.H. Liu, and Z.H. Peng, Thermodynamic model for equilibrium solubility of gibbsite in concentrated NaOH solutions, *Trans. Nonferrous Met. Soc. China*, 22(2012), No. 2, p. 447.

[13] J.A.M. Pereira, M. Schwaab, E. Dell'Oro, J.C. Pinto, L.F. Monteiro, and C.A. Henriques, The kinetics of gibbsite dissolution in NaOH, *Hydrometallurgy*, 96(2009), No. 1-2, p. 6.

[14] J. Addai-mensah, J. Dawe, and J. Ralston, The dissolution and interactions of gibbsite particles in alkaline media, *Dev. Miner. Process.*, 13(2000), p. C6-1.

[15] L. Bao, T.A. Zhang, Y. Liu, Z.H. Dou, G.Z. Lü, X.M. Wang, J. Ma, and X.L. Jiang, The most probable mechanism function and kinetic parameters of gibbsite dissolution in NaOH, *Chin. J. Chem. Eng.*, 18(2010), No. 4, p. 630.

[16] A.J. Yin, Q.Y. Chen, and P.M. Zhang, Studies on the kinetics of dissolution process of synthetic gibbsite by DSC, *Chem. Res. Chin. Univ.*, 12(1991), No. 11, p. 1507.

[17] C.Q. Li, P.M. Zhang, Q.Y. Chen, and X.M. Chen, Investiga-

tion of dissolution process kinetics of gibbsite, *Nonferrous Met.*, 43(1991), No. 4, p. 52.

[18] Y.X. Hua, *Introduction to Metallurgical Process Dynamics*, Metallurgical Industry Press, Beijing, 2004, p. 188.

[19] H.G. Li, *Hydrometallurgy*, Central South University Press, Changsha, 2005, p. 69.

[20] H.B. Yang, X.L. Pan, H.Y. Yu, G.F. Tu, and J.M. Sun, Dissolution kinetics and mechanism of gibbsitic bauxite and pure gibbsite in sodium hydroxide solution under atmospheric pressure, *Tran. Nonferrous Met. Soc. China*, 25(2015), No. 12, p. 4151.

[21] H.B. Yang, X.L. Pan, H.Y. Yu, G.F. Tu, and J.M. Sun, Effect of ferrite content on dissolution kinetics of gibbsitic bauxite under atmospheric pressure in NaOH solution, *J. Cent. South Univ.*, 24(2017), No. 3, p. 489.

[22] H.B. Yang, G.F. Tu, X.L. Pan, H.Y. Yu, and J. Hu, Dissolution kinetics of high iron gibbsitic bauxite, *Nonferrous Met. Extract. Metall.*, 2016, No. 2, p. 19.